

3DMPE: 3D Multi-Perspective Embedding

Vahan Huroyan¹, Md Rahat-uz-Zaman², and Stephen Kobourov³

¹ Saint Louis University, St. Louis MO 63103, USA

`vahan.huroyan@slu.edu`

² University of Utah,

`rahat.zaman@utah.edu`

³ Technical University of Munich,

`stephen.kobourov@tum.de`

Abstract. We study 3D point cloud reconstruction from multiple partially observed 2D projections. Given two or more projections of an unknown 3D point cloud, together with cross-view point correspondences and visibility information, our goal is to recover a consistent 3D configuration when different views contain different subsets of points. We propose *3D Multi-Perspective Embedding* (3DMPE), an optimization-based, training-free method that reconstructs the 3D point cloud and, in the variable-projection setting, jointly estimates the projection maps. 3DMPE extends Multi-Perspective Simultaneous Embedding to accommodate missing points and incomplete pairwise distance information across views. We consider both fixed-projection and variable-projection settings. Unlike learning-based reconstruction methods that infer shape from raw images and often depend on training data, 3DMPE operates on geometric observations with established correspondences and does not require category-specific training. Experiments on ShapeNet and Pix3D evaluate reconstruction quality using Chamfer Distance, Earth Mover Distance, and RMSE-Optimize-Align (ROA), and examine the effects of initialization, the number of views, point visibility, and several noise regimes, including noisy distances and erroneous correspondences. The results demonstrate that 3DMPE can effectively reconstruct point clouds from partial multi-view geometric observations.

Keywords: 3D Point Cloud Reconstruction · Multi-View Geometry · 3D Reconstruction

1 Introduction

Understanding the 3D structure of objects from limited observations is a fundamental problem in computer vision, with applications in robotics, autonomous driving, precision agriculture, gaming, and virtual and augmented reality. The 3D reconstruction problem aims to infer the three-dimensional structure of an object or scene from one or more 2D images. In general, this problem is ill-posed and highly sensitive to noise and missing information. In the noise-free case, the problem is called triangulation [15]. Yet, noise is unavoidable. Our setup assesses how different noise regimes affect our algorithm’s performance.

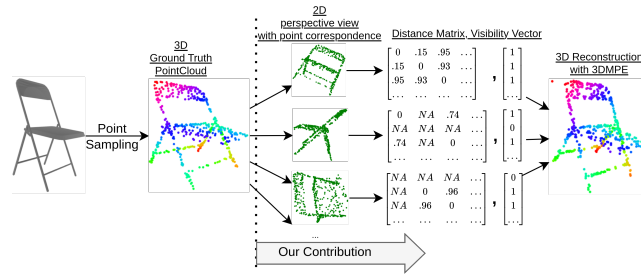


Fig. 1: Full pipeline of 3DMPE. Given multiple 2D snapshots and the visibility vectors (1 if a point is present in a view and 0 otherwise), in this example 3, but the algorithm works for arbitrary number of inputs, we first compute the pairwise distance matrices for each snapshot the algorithm reconstructs the 3D point cloud.

In practice, 3D reconstruction is often addressed using Structure-from-Motion (SfM) pipelines [3, 13, 31], which process raw images through feature detection, correspondence matching, camera pose estimation, and triangulation. Modern systems such as COLMAP [36] provide end-to-end implementations of this pipeline and are widely used in practice.

In this work, we study a more structured reconstruction problem corresponding to the geometric recovery stage after point correspondences have been established. Specifically, the input consists of multiple partially observed 2D projections of an unknown 3D point cloud, together with point-to-point correspondences and visibility information across views. A point may be absent from some views because of occlusion or limited visibility, and consequently the pairwise distance information is incomplete. We do not address feature detection or correspondence estimation from raw images; instead, we study how accurately the underlying 3D point cloud can be recovered once these geometric observations are available.

Our formulation also considers two settings. In the fixed-projection setting, the projection viewpoints are given as part of the input. In the variable-projection setting, the viewpoints are unknown and must be estimated jointly with the 3D point cloud. The goal in both cases is to recover 3D coordinates that are consistent with all observed 2D distances.

To address this problem, we propose *3-Dimensional Multi-Perspective Embedding* (3DMPE), an optimization-based method for reconstructing 3D point clouds from multiple partially observed 2D projections. 3DMPE is inspired by Multi-Perspective Simultaneous Embedding (MPSE) [16], which jointly embeds multiple datasets described by pairwise distance matrices. However, standard MPSE assumes complete pairwise distance information in every view and therefore cannot be directly applied when points are absent from some projections. We modify the MPSE objective to explicitly account for visibility and missing pairwise distances, thereby enabling reconstruction from partial observations.

Unlike learning-based methods [9, 26, 47] that infer 3D shape from raw images, 3DMPE does not require object-specific training data. Instead, it exploits

geometric consistency across views once correspondences are available. Thus, the two classes of methods address complementary input settings rather than being directly comparable in all experimental regimes.

Our main contributions are:

- We formulate 3D point cloud reconstruction from partially observed 2D projections with known correspondences and visibility information.
- We introduce 3DMPE, including fixed-projection and variable-projection formulations that extend MPSE to incomplete distance observations.
- We evaluate the method on ShapeNet [4] and Pix3D [43] and study its behavior under changes in initialization, number of views, point visibility, input size, and several noise models.

Fig. 1 illustrates the 3DMPE pipeline.

2 Related Work

The 3D reconstruction problem has been studied for several decades. The timeline can be generally split into two periods: focus on understanding the geometry and the structure of the 3D object from given 2D images, followed by deep learning methods; see survey by Han et al. [14]. The first period includes Stereo-based approaches [15], PDE-based approaches [57], and SfM [3, 13, 31, 36]. For such methods, a final step often involves surface reconstruction from point clouds, as discussed by Berger et al. [2].

The second period is characterized by deep learning methods, starting with voxel-based volumetric representations of 3D objects. Wu et al. [50] represent a geometric 3D shape as a probability distribution on a voxel grid and uses a convolutional deep belief network for the reconstruction. Wu et al. [49] propose a model by leveraging volumetric convolutional networks and generative adversarial networks. Gidhar et al. [11] propose a TL-embedding network to reconstruct volumetric shapes from RGB images. Tatarchenko et al. [44] use an octree representation along with deep convolutional decoder architecture to generate volumetric 3D outputs. Other directions of voxel-based multi-view and single-view reconstruction are introduced by Kar et al. [18] and Tulsiani et al. [45].

Recent work in this domain explores surface-based representations. Fan et al. [9] propose a PSGN architecture (loss function and learning paradigm), to predict multiple plausible 3D point clouds from an input image. Mandikal et al. [26] propose an auto-encoder based approach, where instead of learning just one reconstruction, they predict multiple reconstructions that are consistent with the input view. Haoqiang et al. [9], Insafutdinov and Dosovitskiy [17] train a convolutional network for shape and make predictions from a single image by minimizing the reprojection error. Lin et al. [23] use 2D convolutional operations for the 3D structure prediction task from multiple viewpoints. Sridhar et al. [41] propose a dense 3D shape reconstruction from a variable number of RGB views of previously unobserved object instances. Mandikal and Babu [27] propose a deep pyramidal network for point cloud reconstruction.

Miclea et al. [29], Cheng [5], Hamid et al. [12], Altingövde [1] and Neubert et al. [30] study the 3D reconstruction task from the output of active stereo vision systems, where the input is only limited to two images, taken from nearby positions. Other approaches to this and related problems include Michalkiewicz et al. [28], who use a linear decoder, obtained from the PCA on the signed distance function of the surface, to obtain the 3D reconstruction. Lei et al. [21] design a neural network that generates high-quality parametric 3D surfaces that are consistent between the given views. Klovov et al. [19] propose a probabilistic reconstruction network which expresses image-conditioned 3D shape inference through a family of latent variable models. Choy et al. [6] propose a unified approach for single and multi-view 3D object reconstruction. Their proposed RNN architecture learns a mapping from a set of images of objects to their 3D shapes. Rocco et al. [33], Seki et al. [37], Zbontar et al. [53] and Zhu et al. [56] use deep neural network for matching feature points in images to find correspondences. Recent methods such as DUS3R [47], MAST3R [22], and VGGT [46] jointly estimate correspondences and geometric information from images. These methods are complementary to 3DMPE and could provide the correspondences or geometric observations required by our optimization-based framework.

One drawback of such deep learning methods is that they work well only on objects similar to those in the training sets. Such several approaches to reconstruct/estimate human hands include [20, 52]. To be successful, such methods need large and diverse training data. We remark, that our approach does not require a training data and we do not learn a specific type of object. Instead, we require multiple snapshots of the object with some registered annotations on it and our proposed algorithm manages to find an embedding for these annotation points in 3D that recover the 3D structure of the underlying object.

2.1 Multi-Perspective Simultaneous Embedding

Here we summarize MPSE [16], which aims to visualize datasets and graphs based on multiple pairwise distances between its instances. The goal of MPSE is to compute coordinates of points in 3D, as well as provide different views into the data, by means of 2D projections that preserve each of the given distance matrices. Given K matrices $D^{(1)}, \dots, D^{(K)}$ of size $N \times N$ with non-negative entries, also referred to as the **pairwise distance matrices**, MPSE aims to find $\{x_1, \dots, x_N\} \in \mathbb{R}^3$ as well as K possible subspaces (or orthogonal projection matrices $P^{(1)}, \dots, P^{(K)}$), such that the distances between i -th and j -th points in k -th pairwise distance matrix $D_{ij}^{(k)}$ is well approximated by the distance between x_i and x_j in the corresponding k -th subspace. That is, $\|P^{(k)}x_i - P^{(k)}x_j\|$ is as close to $D_{ij}^{(k)}$ as possible for $1 \leq k \leq K$ and $1 \leq i, j \leq N$. MPSE achieves this goal with the help of the multi-perspective MDS stress function:

$$S(\mathcal{X}, \mathcal{P}; \mathcal{D}) = \sum_{k=1}^K \sum_{i>j} \left(\mathbf{D}_{ij}^{(k)} - \|P^{(k)}(x_i) - P^{(k)}(x_j)\| \right)^2 \quad (1)$$

The minimizer ($\{x_1, x_2, \dots, x_N\} \subset \mathbb{R}^3$) of (1) is the solution of MPSE based on the given distance matrices. There are two variants of MPSE: fixed projections (the projection viewpoints are given) and variable projections (the projection viewpoints are unknown). With fixed projections the projection subspaces are part of the input and MPSE only minimizes (1) with respect to $\{x_1, x_2, \dots, x_N\}$. MPSE with variable projections finds the coordinates $\{x_1, x_2, \dots, x_N\}$ along with best possible subspaces (projections) $P^{(1)}, P^{(2)}, \dots, P^{(K)}$ for which the pairwise distance matrices are well approximated.

3 3D Multi-Perspective Embedding

In this section, we describe our 3-Dimensional Multi-Perspective Embedding (3DMPE) approach for 3D point cloud reconstruction. Recall, that we assume multiple 2D viewpoints of an unknown 3D point cloud. For each 2D point cloud, we compute pairwise distance matrices for the visible points. As different subsets of points are hidden in different views, we need to handle pairwise distance matrices with missing entries. A hidden (missing) point implies that the entire corresponding row and column are missing from the pairwise distance matrix.

We formally define the 3DMPE problem as follows. Let N be the number of points in the unknown 3D point cloud that 3DMPE must reconstruct, given K 3D viewpoints captured by pairwise distance matrices between subsets of points, $\mathbf{D}^{(1)}, \dots, \mathbf{D}^{(K)}$ (different entries missing in different matrices due to occlusion). Define a visibility vector $\alpha^k \in \mathbb{R}^N$ for each view $1 \leq k \leq K$, where $\alpha_i^{(k)} = 1$ if the i -th keypoint is present in the k -th view and $\alpha_i^{(k)} = 0$ otherwise. 3DMPE minimizes the stress function below:

$$S_{3DREC}(\mathcal{X}, \mathcal{P}; \mathcal{D}) = \sum_{k=1}^K \sum_{i>j} \alpha_i^{(k)} \alpha_j^{(k)} \left(\mathbf{D}_{ij}^{(k)} - \|P^{(k)}(x_i) - P^{(k)}(x_j)\| \right)^2. \quad (2)$$

Similar to MDS and MPSE, 3DMPE is also a non-convex problem. We remark, that if i -th and j -th points are present in k -th view then both α_i^k and α_j^k are 1 and their product is also 1. Otherwise (when either or both i -th or j -th points are missing from the k -th view), $\alpha_i^{(k)} \alpha_j^{(k)} = 0$.

The optimization problem in (2) can be considered in two different scenarios. The first and more simple scenario, which we refer to as reconstruction for fixed projections, assumes that we are given the viewpoints, that is we are given the projection matrices $P^{(1)}, \dots, P^{(K)}$ and we only need to optimize over the x_1, \dots, x_N . The optimization problem for this case is

$$\arg \min_{\mathcal{X}} S_{3DREC}(\mathcal{X}, \mathcal{P}; \mathcal{D}) \quad (3)$$

The second scenario is more complex, we refer to it as reconstruction for varying projections, which assumes that the projection matrices $P^{(1)}, \dots, P^{(K)}$ are also variable:

$$\arg \min_{\mathcal{X}, \mathcal{P}} S_{3DREC}(\mathcal{X}, \mathcal{P}; \mathcal{D}) \quad (4)$$

Algorithm 1 3DMPE for Fixed Projections by SGD

Require: Pairwise Distance Matrices: $\mathcal{D} = \{\mathbf{D}^{(1)}, \dots, \mathbf{D}^{(K)}\}$,
 Visibility vectors $\{v^{(1)}, \dots, v^{(K)}\}$,
 Initial embedding \mathbf{X}_0 , initial learning rate μ_0 , stochastic constant c , iteration number T , projection matrices P .
for $t = 1, 2, \dots, T$ **do**
 $\xi_t \sim \Xi(\mathbf{D}, c)$
 $\mathbf{X}_t = \mathbf{X}_{t-1} - \mu_{t-1} \nabla_{\mathbf{X}} S_{\xi_t}^2(\mathbf{X}_{t-1}, \mathbf{P}; \mathbf{D})$
 $\mu_t = \mu(\mathbf{X}_{t-1}, \mathbf{X}_t, \xi_t)$
end for
Ensure: \mathbf{X}_T

Algorithm 2 3DMPE with varying perspectives by SGD

Require: Pairwise Distance Matrices: $\mathcal{D} = \{\mathbf{D}^{(1)}, \dots, \mathbf{D}^{(K)}\}$,
 Initial embedding, perspective parameters: \mathbf{X}_0 ,
 \mathbf{Q}_0 , Visibility vectors $\{v^{(1)}, \dots, v^{(K)}\}$, Initial learning rates $\mu_{\mathbf{X}}$, and $\mu_{\mathbf{Q}}$, Stochastic constant: c , iteration number: T .
for $t = 1, 2, \dots, T$ **do**
 $\xi_t \sim \Xi(\mathbf{D}, c)$
 Compute $\nabla S_{\xi}^2(X_{t-1}, \mathbf{Q}_{t-1})$ and $\nabla S_{\xi}^2(X_t, \mathbf{Q}_t)$
 Compute μ_t .
 $\mathbf{X}_t = \mathbf{X}_{t-1} - \mu_{\mathbf{X},0} \nabla_{\mathbf{X}} S_{\xi}^2(\mathbf{X}, \mathbf{Q}_t)$.
 $\mathbf{Q}_t = \Pi(\mathbf{Q}_t - \mu_{\mathbf{Q},t} \nabla_{\mathbf{Q}} S_{\xi}^2)$
 $\mu_t^{\mathbf{X}} = \mu(\mathbf{X}_{t-1}, \mathbf{X}_t, \xi_t)$
 $\mu_t^{\mathbf{Q}} = \mu(\mathbf{Q}_{t-1}, \mathbf{Q}_t, \xi_t)$
end for
Ensure: $X_{\text{final}}, \mathbf{Q}_{\text{final}}$.

To solve (3) and (4) we use Stochastic Gradient Descent (SGD) [32] with smart initialization, which is also used as baseline; see Sec. 3.3.

3.1 Algorithm

The 3DMPE algorithms (fixed projections and variable projections) are summarized in Algorithm 1 and Algorithm 2, respectively. The algorithmic details are discussed in Sec. 3.2. We use smart initialization for the initial 3D embedding and minibatch SGD with early termination [51] on the gradient and stress values. Implementation details are discussed in Sec. 4.5, dataset details are in Sec. 4.1 and evaluation details are in Sec. 3.3.

3.2 Details of Algorithms 1 and 2

Algorithms 1 and 2 are described in Sec. 3.1 and here we provide some additional details. Similar to MPSE [16], the objective functions for fixed projections (3) and varying projections (4) are non-convex. Thus, a gradient descent algorithm

is not guaranteed to find the global minimum. A good implementation of SGD, however, has been shown to consistently find high quality solutions [55]. We use SGD with smart initialization to solve the optimization problems in (3) and (4). SGD uses the following sampling mechanism: First, we define the following random variable $\xi \sim \Xi(\mathbf{D}, c)$, which samples an incomplete pairwise dissimilarity matrix based on a given dissimilarity matrix \mathbf{D} . That is, ξ itself is a pairwise distance matrix, for which, each entry of \mathbf{D} is included in ξ with probability c ; otherwise, it is 0. Based on this sample from the pairwise distance matrix, we define:

$$S_\xi(\mathcal{X}, \mathcal{P}; \mathcal{D}) = S_{3DREC}(\mathcal{X}, \mathcal{P}; \xi). \quad (5)$$

Note, that here $\xi = [\xi^1, \dots, \xi^K]$, and for $1 \leq k \leq K$, $\xi^k \sim \Xi(\mathbf{D}^k, c)$. Similar to [16], the adaptive step size is chosen by adaptive scheme [25]. For Algorithm 1, the adaptive step size $\mu_{\mathbf{X}}$ is defined as:

$$\mu_{\mathbf{X}}(\mathbf{X}_t, \mathbf{X}_{t-1}, \xi_t) = \frac{(\mathbf{X}_t - \mathbf{X}_{t-1})^T \left(\nabla_{\mathbf{X}} S_{\xi_t}^2(\mathbf{X}_t, \mathcal{P}; \mathcal{D}) - \nabla_{\mathbf{X}} S_{\xi_t}^2(\mathbf{X}_{t-1}, \mathcal{P}; \mathcal{D}) \right)}{\left\| \nabla_{\mathbf{X}} S_{\xi_t}^2(\mathbf{X}_t, \mathcal{P}; \mathcal{D}) - \nabla_{\mathbf{X}} S_{\xi_t}^2(\mathbf{X}_{t-1}, \mathcal{P}; \mathcal{D}) \right\|^2}, \quad (6)$$

where $\mathbf{X}_t, \mathbf{X}_{t-1}$ are the embeddings at steps t and $t-1$, ξ_t are the sampled pairwise distance matrices at iteration $1 \leq t \leq T$ and $\nabla_{\mathbf{X}} S_{\xi_t}^2(\mathbf{X}_t)$ is the gradient of $S_{\xi_t}^2$ at iteration $1 \leq t \leq T$. For Algorithm 2, μ_t^Q is defined similarly.

3.3 Baseline Approach and Evaluation Metrics

We propose the following basic 3D point cloud reconstruction idea from given 2D projections as a baseline approach: Given multiple pairwise distance matrices, we suggest computing their average and using Multi-Dimensional Scaling (MDS) [38] to embed the point cloud in 3D based on the combined proximity distance matrix. We refer to this reconstruction as the **baseline** reconstruction and use it to compare against 3DMPE. To initialize the 3DMPE algorithm for stochastic gradient descent (SGD), we have two options: random initialization, referred to as 3DMPE with random initialization, or use the baseline method to initialize the SGD, which we call 3DMPE with smart initialization. We will compare these two approaches in later sections. In Sec. 4.2 we numerically demonstrate the effect of smart initialization on the performance of 3DMPE.

We use two standard metrics to evaluate the quality of the 3D point cloud reconstruction when compared to the underlying 3D point cloud: The Earth Mover Distance (EMD) [34] between point clouds X and \hat{X} is defined as:

$$d_{EMD}(X, \hat{X}) = \min_{\phi: X \rightarrow \hat{X}} \sum_{x \in X} \|x - \phi(x)\|_2 \quad (7)$$

where $\phi: X \rightarrow \hat{X}$ is a bijection.

The second one is the Chamfer Distance (CD) between point clouds X and \hat{X} is defined as:

$$d_{CD}(X, \hat{X}) = \sum_{x \in X} \min_{\hat{x} \in \hat{X}} \|x - \hat{x}\|_2^2 + \sum_{\hat{x} \in \hat{X}} \min_{x \in X} \|x - \hat{x}\|_2^2. \quad (8)$$

Note that neither metric (EMD and CD) takes into account rotations and translations, thus requiring an initial alignment of the two point clouds. The Iterative Closest Point (ICP) [54] algorithm is often used for such alignments, e.g., [26]. As ICP can get stuck in local minima, we improve the alignment by point-to-point correspondence information. Specifically, we align 4 points using (9).

$$T = AX^{-1}, \quad (9)$$

where A and X are the 4 selected points from the two point clouds in $\mathbb{R}^{4 \times 4}$ and T is the corresponding transformation matrix in $\mathbb{R}^{4 \times 4}$ for homogeneous points. Using RANSAC [10], this process is repeated 1000 times, by selecting T that minimizes (10):

$$\mathcal{L}(x, y) = \frac{\sum \|x_i - y_i\|_2}{n} \quad (10)$$

In addition to the EMD and CD metrics, we also use a customized RMSE-Optimize-Align (ROA) metric; see Fig. 2. Given two point clouds, X and \hat{X} we compute the Root-Mean-Square Error (RMSE) for all corresponding pairs of points, with the best possible homogeneous space transformation matrix T applied to the points of \hat{X} . The optimization problem to align the points can be written as:

$$RMSE^2 = \min_T \frac{1}{N} \sum_{i=1}^N \|X_i - T\hat{X}_i\|_2^2. \quad (11)$$

The problem can be tackled with SGD on the objective function. A closed form solution to RMSE can be given by SVD; see the Appendix.

4 Experiments

We evaluate 3DMPE in both the fixed and variable-projection settings on the ShapeNet and Pix3D datasets. Our experiments address four questions: (i) how accurately does 3DMPE reconstruct 3D point clouds relative to our MDS-based baseline; (ii) how do initialization, the number and diversity of views, point visibility, and point-cloud size affect reconstruction quality and runtime; (iii) how robust is the method to noisy distances and erroneous correspondences; and (iv) how can 3DMPE be used within an image-based reconstruction pipeline.

Unless stated otherwise, we run minibatch SGD for at most 300 iterations and terminate early when either the objective value or gradient norm falls below (10^{-4}) . We use Chamfer Distance (CD), Earth Mover Distance (EMD), and ROA, as defined in Sec. 3.3, to evaluate reconstruction quality. Our primary

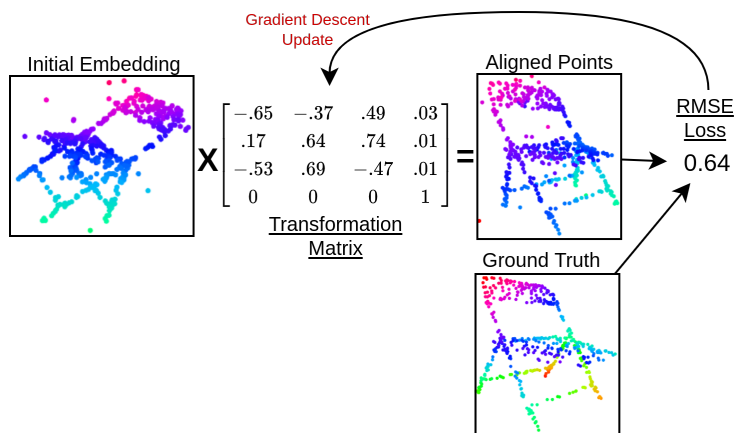


Fig. 2: Pipeline for ROA metric. Here 0.64 is the ROA value for current iteration of gradient descent update loop.

controlled comparison is with the proposed MDS-based baseline. We additionally include published results for learning-based methods and an exploratory comparison with COLMAP for context; these methods use different inputs and assumptions and are therefore not directly comparable to 3DMPE.


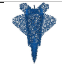


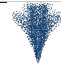












































4.1 Datasets and Experimental Setup

In the experiments reported here, we use the normalized mesh of objects (*.obj* format) from the **ShapeNET** [4] and **Pix3D** [43] datasets. From each 3D object, we uniformly sample dense point clouds of as many points as required by the specific experiment (see [48] for details). Next, we specify the rotation matrices for each projection. The general rotation matrix R by applying rotation angles α , β , and γ in x, y, z axis is given in (12). For the sake of brevity we use $c\theta$ and $s\theta$ to denote $\cos(\theta)$ and $\sin(\theta)$, respectively.

$$R = \begin{bmatrix} c\alpha \cdot c\beta & c\alpha \cdot s\beta \cdot s\gamma - s\alpha \cdot c\gamma & c\alpha \cdot s\beta \cdot c\gamma + s\alpha \cdot s\gamma \\ s\alpha \cdot c\beta & s\alpha \cdot s\beta \cdot s\gamma + c\alpha \cdot c\gamma & s\alpha \cdot s\beta \cdot c\gamma - c\alpha \cdot s\gamma \\ -s\alpha & c\beta \cdot s\gamma & c\beta \cdot c\gamma \end{bmatrix} \quad (12)$$

Assuming that we need to generate K projections from the angle range $[\theta_s, \theta_e]$ in all axes, we need 3 angles, α_k , β_k and γ_k , for $1 \leq k \leq K$. We assume the band of angle in all axes is $\theta_r = \theta_e - \theta_s$. For $1 \leq k \leq K/2$, we randomly select the angles from range $[(k-1) \cdot \theta_r / K, k \cdot \theta_r / K]$. We do the same for $K/2 < k \leq K$ but for negated angles, so the range is $[-((k-K/2)-1) \cdot \theta_r / K, -(k-K/2) \cdot \theta_r / K]$ (when K is odd, we apply the same process for $K+1$ and discard the last one). We also record the negations of these angles, as they are the input for 3DMPE with fixed projections. Unless stated otherwise, $\theta_s = 0^\circ$ and $\theta_e = 360^\circ$.

Table 1: 3D reconstruction results for qualitative comparison between 3DMPE with fixed angle projections, PSGN, and 3D-LMNet. The baseline is used from [26].

Input	Ground Truth	PSGN [9]	BL [26]	3D-LMNet [26]	3DMPE(F)	3DMPE(V)
						
						
						
						
						
						
						

We utilize the raytracing algorithm [39] to the transformed point clouds [8] to determine which points will be visible from a specified projection. Note, that not all points are visible in every projection; the ray tracing process helps us identify the visible points. With the rotation matrices already established, we position the rotated point cloud away from the origin while maintaining the viewpoint at the origin, casting rays toward the positive z -axis. We compute the pairwise distance matrices from the output of the raytracing algorithm.

Before raytracing, we assign unique IDs to each point in the point cloud. During raytracing, we keep track of those IDs and keep them for the 2D projections. This way, point-to-point correspondence is reserved. The presence of a point in a perspective is recorded in a visibility vector (1 for presence and 0 for absence); see Fig. 1.

4.2 Experiments on ShapeNet

We run 3DMPE on ShapeNet and report the results below. For comparison, we identify the 3D objects used in the experiments of [26] and use them in both our fixed and variable projections settings. Tab. 1 demonstrates a qualitative comparison of 3DMPE alongside other 3D reconstruction algorithms (with different setups), baseline, as well as the ground truth. Visual inspection suggests that 3D-LMNet and 3DMPE with fixed projection outperform the rest. Tab. 3 confirms the visual observations from Tab. 1 with a quantitative comparison with the CD and EMD metrics.

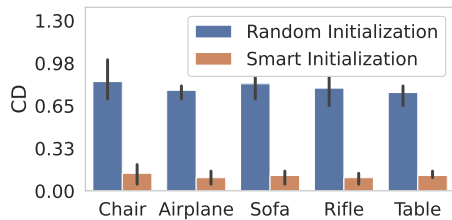
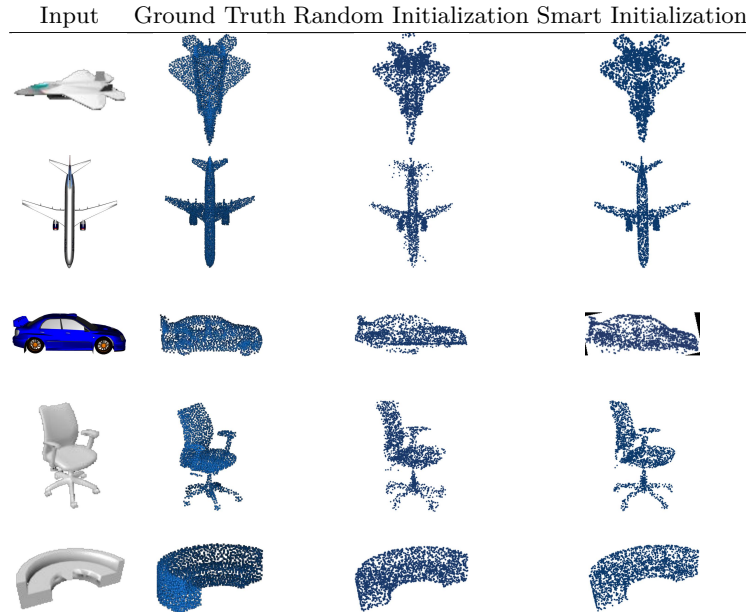


Fig. 3: Effect of initialization: blue corresponds to random and orange to smart initialization.

The Effect of Smart Initialization As the objective functions of 3DMPE with fixed (3) and varying projections (4) are non-convex, initialization is important for the SGD step. In this section we analyze the effect of smart initialization (see Sec. 3.3) on the performance of 3DMPE. We run 3DMPE with smart initialization and compare the results with that of random initialization for the same set of distance matrices. For the random initialization we sample points uniformly at random from a unit cube. For each experiment we take 4 instances from the ShapeNet dataset, sample 1024 points (see Sec. 4.1), set the number of viewpoints to 5 with each point visible from 3 viewpoints, and set the maximum number of iterations per experiment to 200. We repeat each experiment 4 times and report the average CD of reconstructions in Fig. 3, where blue corresponds to smart initialization and orange corresponds to random initialization. We observe that in all experiments smart initialization outperforms random initialization by an order of magnitude. Moreover, the large Chamfer distance (CD) values indicate that random initialization might lead to local rather than global minima. Table 2 shows the 3DMPE reconstruction with and without smart initialization, which visually illustrates this point. We remark that smart initialization not only leads to better reconstruction, but also leads to better running time of the algorithm, as fewer iterations are needed to convergence.

Robustness of the Algorithm For all experiments in this section, we take 5 instances from the ShapeNet and sample $n = 1024$ points, with 5 viewpoints, where each point is visible from 3 viewpoints. We have observed that the threshold value for CD under which the reconstruction is acceptable is ≈ 0.2 ; see Fig. 4a and Fig. 4b.

We analyze the performance of 3DMPE under various noise regimes. First, we consider additive Gaussian noise to the pairwise distance matrices. We compute the corresponding pairwise distance matrices and add Gaussian noise to them as follows: For a given noise amplitude $0 \leq p \leq 1$ we uniformly pick nq rows in distance matrices and add them Gaussian noise, $\mu = 0$, $\sigma^2 = pd$, where d is the diameter of the point cloud. We substitute the negative values by 0 and make the matrices symmetric. Next, we run 3DMPE with varying projections for these corrupted pairwise distance matrices and report the average reconstruction CD values in Fig. 4a. For p in the range $[0.05, 0.1]$, increasing the percentage of

Table 2: Example of different 3D objects from ShapeNet dataset with Random and Smart Initialization. The iterations of all experiments are limited to 200.**Table 3:** Demonstration of the 3DMPE algorithm (last 2 columns) for 8 different 3D models from the Shapenet dataset. For each, 2048 points are used with 4 viewpoints. Projections are created with a raytracing algorithm.

Category	Chamfer						EMD					
	Baseline [26]	PSGN [9]	3D-LMNet [26]	Our BL	3DMPE(F)	3DMPE(V)	Baseline	PSGN	3D-LMNet	Our BL	3DMPE(F)	3DMPE(V)
airplane	3.61	3.74	3.34	3.41	0.55	1.58	7.42	6.38	4.77	4.86	0.02	1.41
bench	4.70	4.63	4.55	3.89	1.07	1.94	5.66	5.88	4.99	4.09	1.25	1.65
car	4.67	5.20	4.55	4.34	1.02	4.01	4.74	4.87	4.10	3.8	0.01	4.64
chair	6.51	6.39	6.41	5.41	1.85	4.28	8.99	9.63	8.02	3.73	1.03	1.21
lamp	7.32	6.33	7.10	7.47	3.14	6.36	20.96	16.17	15.8	9.42	2.86	7.01
rifle	2.99	2.91	2.75	2.22	2.11	2.14	9.30	8.48	6.08	2.45	0.72	1.94
sofa	6.11	6.98	5.85	5.70	0.06	0.39	6.40	7.42	5.65	4.32	0.03	0.06
table	6.16	6.00	6.05	6.10	1.27	2.01	9.51	8.40	7.82	4.85	1.99	2.68
mean	5.99	5.54	5.40	4.82	1.56	2.84	7.82	7.20	7.00	4.69	0.99	2.58

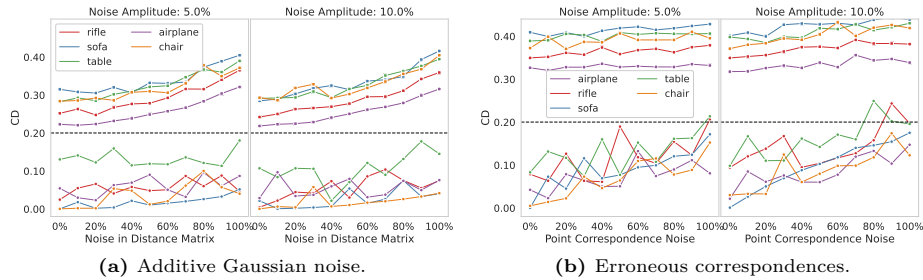


Fig. 4: Noise robustness analysis of 3DMPE (1024 points, 5 viewpoints). x -axis shows the percentage of corrupted points. Top curves: baseline model (squares); bottom curves: 3DMPE (circles).

corrupted points results in a slight increase in CD values while staying in the desired range, i.e., the algorithm successfully recovers the shapes. In Fig. 4a we also report the values achieved by the baseline model for the experiment with square marked lines and note that the decrease in accuracy for the baseline model is much higher.

Next, we analyze the performance of 3DMPE under erroneous correspondences. Given $0 \leq q \leq 1$ (the fraction of points we aim to corrupt), we randomly pick nq points and change the correspondence to a random point, at most pd distance away from it in 3D space, where d is the diameter of the point cloud. We compute the pairwise distance matrices and run 3DMPE with varying projections; see Fig. 4b: the x -axis corresponds to the value of q , the left subfigure corresponds to $p = 0.05$ and the right one corresponds to $p = 0.1$. We observe that 3DMPE is robust to inaccuracies in correspondences: even when almost all correspondences are wrong, as long as they are in some reasonable range, 3DMPE recovers the 3D point cloud.

Scalability of the Algorithm We next discuss the performance of 3DMPE (in both the fixed and variable projections setting) with different size point clouds, with different number of viewpoints, with respect to accuracy and runtime. Fig. 5a and Fig. 5b demonstrate the effect on runtime with more viewpoints for fixed and variable projections, respectively.

In the fixed embedding setting, the effect of increasing the projections (from 2 to 8) is negligible. In the variable embedding setting there is an increase in runtime that is linear in the number of viewpoints (as in this setting the optimization needs to not only place the points but compute the viewpoints). Fig. 5c and Fig. 5d demonstrate the change in runtime of 3DMPE with fixed and varying projections as the number of points in the input point cloud increases. Clearly the algorithm slows down for larger instances to around 50 seconds for instances with 2048 points in the fixed setting and around 200 seconds in the variable setting.

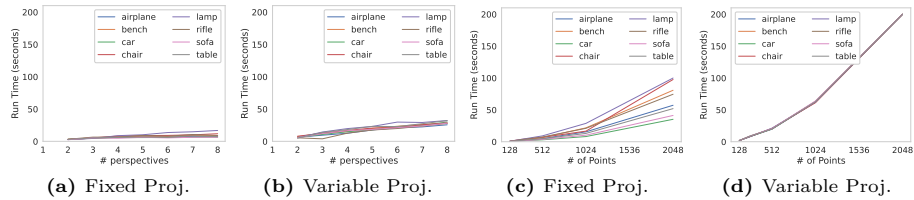


Fig. 5: Runtime (seconds) of 3DMPE with the ShapeNet dataset: (a-b) show the impact of changing the number of perspectives (using 512 points) and (c-d) show the impact of changing the number of points (with 4 projections).

We note that 3DMPE with variable projections solves a more difficult optimization task and requires a greater number of iterations than the fixed projection setting. In this proof-of-concept implementation, we did not invest effort in optimizing 3DMPE for speed.

Although the runtime of 3DMPE is affected by increasing the number of points and viewpoints, we see no significant effect of these parameters on the accuracy of the 3DMPE for both fixed and variable settings; see Fig. 6. Further, the CD, EMD and ROA values for both 3DMPE variants are comparable, although 3DMPE with varying projections is a more complex problem to solve. Fig. 7 demonstrates the effect of the increase of the number of perspectives on CD and EMD when the number of points is fixed. ROA metrics for the same experiments are in the appendix. As expected, reconstruction quality is poor with fewer than 3 perspectives. Typically 4 or 5 projections from different angles suffice for high-quality reconstruction.

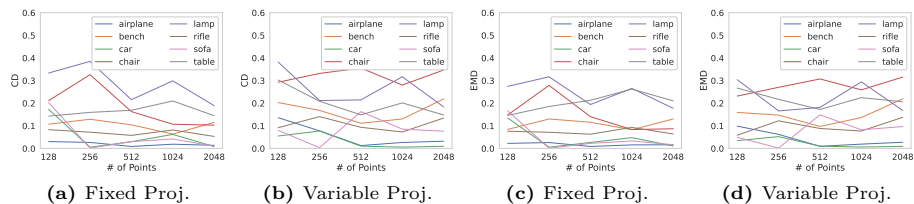


Fig. 6: EMD and CD values with varying number of points on ShapeNet (4 viewpoints, each point visible from 3+ viewpoints).

We analyze the sensitivity of 3DMPE to the percentage of hidden points as follows: fix a parameter ϑ , which represents the number of points that we want to be visible in each projection, create the 2D projections from the given point cloud, and from each projection remove $N - \vartheta$ point at random. In Fig. 8 we report the CD and EMD (ROA data in the appendix) for the point clouds generated by 3DMPE (with fixed and varying projections) for 512 points, ensuring that each point is visible in 1 fewer than the total number of viewpoints (ex-

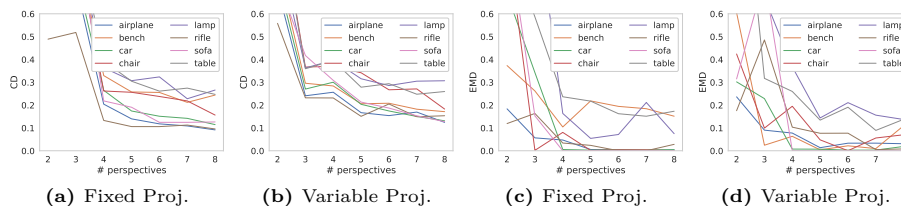


Fig. 7: 3DMPE metrics on ShapeNet for varying viewpoints (512 points; all visible for 23 views, otherwise each point appears in one fewer view).

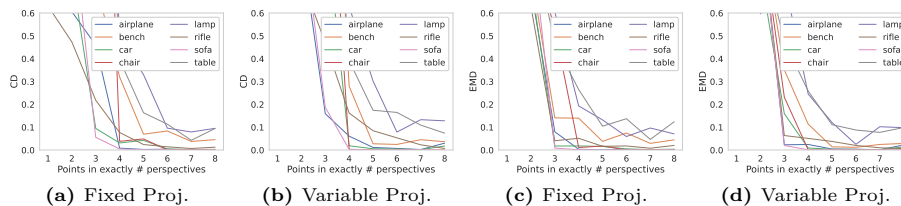


Fig. 8: Metric analysis of 3DMPE on ShapeNet dataset for points visible in a number of viewpoints. All experiments are done for 512 points with 8 viewpoints.

cept 2 and 3 where all points are visible). The experiments show that 3DMPE reconstructs the 3D point cloud properly if each point is visible from at least 3 projections. We remark, that this is feasible in real scenarios of photography. As demonstrated in Fig. 9, even only for 5 projections, most of the points are present in at least 3 viewpoints. Thus, if there are more projections, the points will be visible from at least 3 viewpoints.

Analysis of Angle Constraints. Here we briefly discuss the impact of angle constraints on the 3DMPE algorithm. We choose four 3D models and conduct an experiment where everything else is the same, except for the viewpoint angle constraints. For each experiments, point are visible in exactly 3 projections out of 5. Instead of using $\theta_s = 0$ and $\theta_e = 2\pi$ (so that $\theta_r = 360^\circ$), we start from $[0, 2\pi]$, (viewpoints can be from any side), and slowly narrow down the range to $[0, 0]$ (viewpoints can only be from one location). Fig. 10 shows the performance of 3DMPE for the four 3D models of the ShapeNet dataset, where the x -axis denotes θ_r . Lines with square markers show the baseline, and lines with round markers show 3DMPE. As discussed in Sec. 4.2 the dashed line represents a margin above which the 3D reconstruction becomes unrecognizable. The figure indicates that for $\theta_r \geq 90^\circ$, 3DMPE can reconstruct the whole object.

4.3 Experiments on Pix3D

In addition to experiments with examples from the ShapeNet dataset we also evaluated 3DMPE on examples from the Pix3D dataset [43]; see Tab. 4. In all

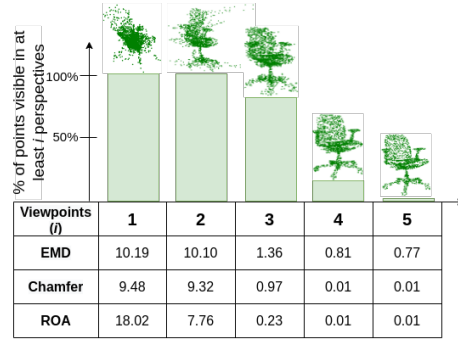


Fig. 9: Points visible in at least 1 . . . 5 viewpoints for ray tracing with five equidistant views. 3DMPE reconstructions for the corresponding points are shown above each bar; reconstruction metrics are reported in the table.

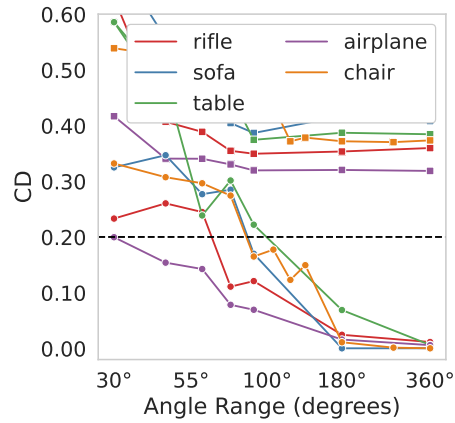


Fig. 10: Performance of 3DMPE with different constraints on viewpoint positions. The x -axis (logarithmic scale) denotes the maximum angle distance between each viewpoint from the center of point cloud.

of these experiments we use 3DMPE with 2048 points and 4 or 5 viewpoints. We remark, that according to our experiments, the quality of reconstruction drastically increases as the number of viewpoints increases. Note, that the exact orientations of the given examples in referred works are unknown. This is possibly due to the fact that these solutions of the 3D point cloud reconstruction problem are based on the relative position of the points rather than the absolute positions of those points. Thus, for both ShapeNet and Pix3D datasets, we visually aligned our baseline and 3DMPE reconstructions as close to the given images as possible. Finally, according to Tab. 4, 3D-LMNet alongside both 3DMPE models performed the best. There are some instances where 3DMPE outperformed 3D-LMNet (e.g., the last table object in Table 4), and some cases where 3DMPE with variable projection performed poorly on certain portions of 3D models (e.g. the 1st sofa of Table 4). This issue is resolved by increasing the number of viewpoints.

Table 4: Demonstration of the 3DMPE algorithm (last 2 columns) for different 3D models from the Pix3D dataset [43]. For all experiments, 2048 points are used with 5 viewpoints. Projections are created with a raytracing algorithm.



















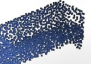






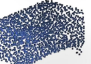




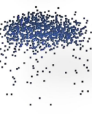











Input	Ground Truth	PSGN	Baseline	3D-LMNet	3DMPE(F)	3DMPE(V)
						
						
						
						
						
						

Table 5: Demonstration of the 3DMPE algorithm (last 2 columns) for 3 different 3D models from the Pix3D dataset. For all experiments, 2048 points are used with 4 viewpoints. Projections are created with raytracing algorithm.

Category	Chamfer						EMD					
	Baseline [26]	PSGN [9]	3D-LMNet [26]	Our BL	3DMPE(F)	3DMPE(V)	Baseline	PSGN	3D-LMNet	Our BL	3DMPE(F)	3DMPE(V)
chair	7.52	8.05	7.35	2.50	1.21	2.15	11.17	12.55	9.14	1.70	1.53	1.74
sofa	8.65	8.45	8.18	3.19	0.53	0.95	8.87	9.16	7.22	2.48	1.01	1.01
table	11.23	10.82	11.20	4.36	3.19	3.98	15.71	15.16	12.73	4.24	3.65	4.11
mean	9.13	9.11	8.91	3.35	1.64	2.36	11.92	12.29	9.70	2.81	2.06	2.29

In Table 5 we present the quantitative comparison between 3DMPE, our proposed Baseline method, and the state-of-art 3D reconstruction models with both metrics CD and EMD. Similar to Tab. 3, we note that 3DMPE with fixed projection performed the best.

Fig. 11 and Fig. 13 demonstrate the performance and runtime metrics for the Pix3D dataset for 3DMPE with both fixed and varying projections. The figures and numbers convey similar impressions to those with the ShapeNet data discussed in Sec. 4.2 (main text).

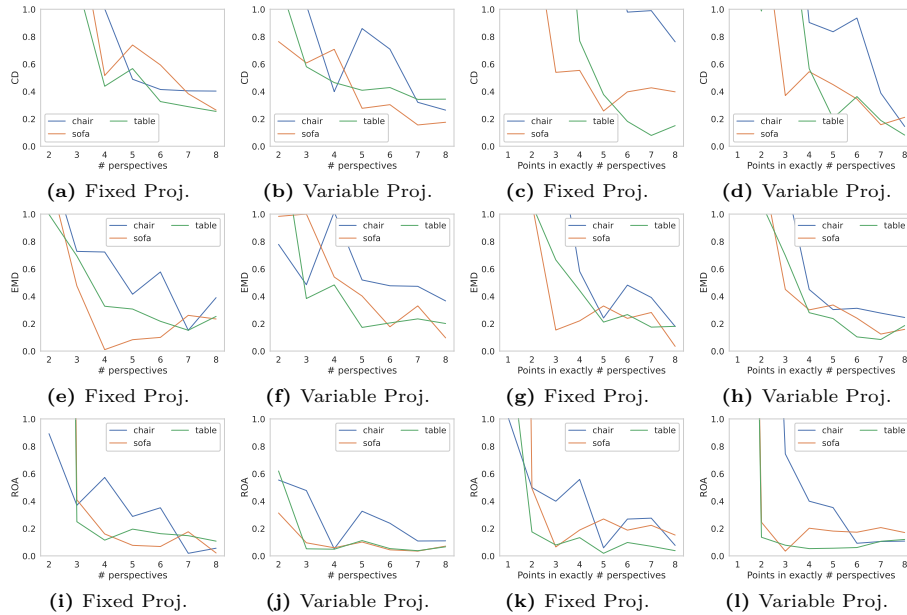


Fig. 11: Metric analysis of 3DMPE on Pix3D dataset for varying viewpoints and visibility of points in those viewpoints. All experiments are done for 512 points. (a-d) shows the metric CD, (e-h) shows EMD and (i-l) shows ROA. For varying number of viewpoints (a-b, e-f, and i-j), each point is visible 1 less than the number of viewpoints (except 2 and 3 where all points are visible).

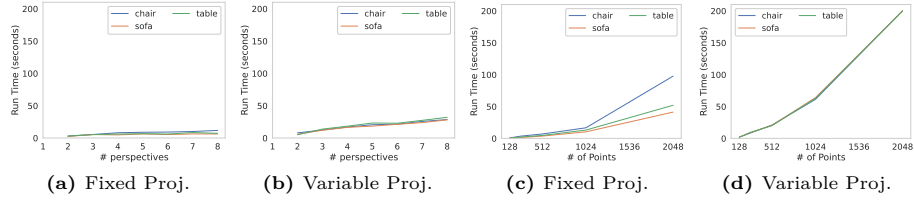


Fig. 12: Runtime (seconds) of 3DMPE on Pix3D dataset: (a-b) show the impact of changing the number of perspectives (using 512 points) and (c-d) show the impact of changing the number of points (with 4 projections).

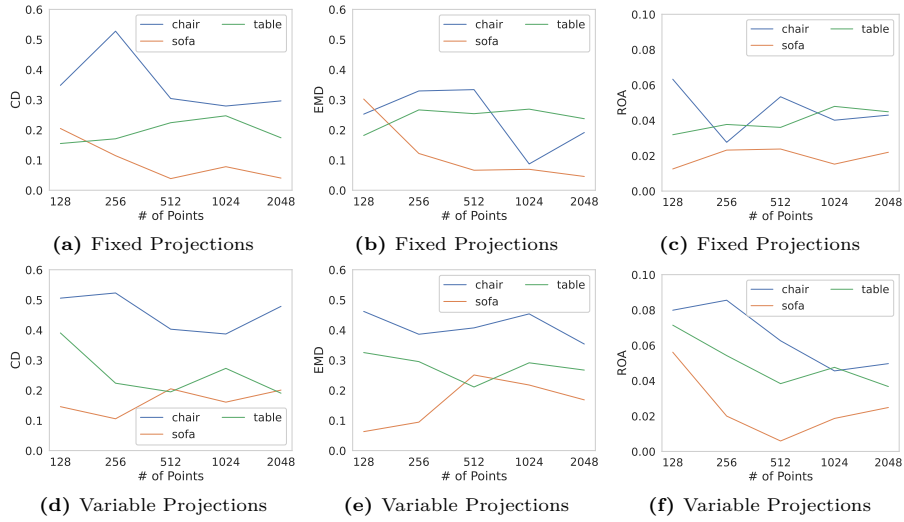


Fig. 13: EMD, CD and ROA metrics on a varying number of points on Pix3D dataset. Each experiment is done with 4 viewpoints and each point is visible from at least 3 viewpoints.

4.4 Exploratory Integration with COLMAP.

COLMAP [36] is a full image-based Structure-from-Motion pipeline, whereas 3DMPE is for point clouds and assumes that point correspondences and visibility information are already available. We therefore explored whether COLMAP could be used to obtain the correspondences required by 3DMPE.

We first applied COLMAP v3.9 to benchmark image collections [35, 40], using its SIFT [24]-based feature extraction and matching pipeline. The resulting feature tracks were sparse, which led to poor 3DMPE reconstructions. Fig. 14 shows the distribution of correspondence counts across 703 images of an airplane model, illustrating that most views contain relatively few matched points.

We next conducted a controlled experiment using a ShapeNet mesh. We rendered 250 images from different viewpoints using Blender [7] and modified the rendering materials to provide sufficient texture variation for feature matching. COLMAP often failed to initialize reliably when fewer than 200 images were used. In contrast, for 3DMPE we generated four partially observed projections and used the known point correspondences inherited from the underlying mesh.

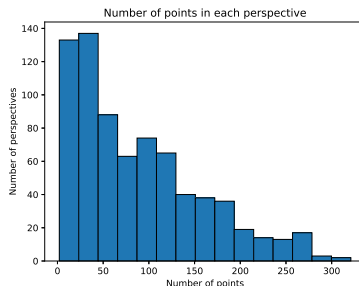






Fig. 14: Maximum correspondences per perspective. With 703 perspectives and 65,373 feature points, the low correspondence count leads to poor reconstruction despite the noise robustness of 3DMPE.

Although the two pipelines use substantially different inputs and assumptions, this experiment illustrates the practical role of correspondence quality. For the selected ShapeNet object, COLMAP reconstructed a point cloud with Chamfer Distance 23.1 using 250 rendered images, whereas 3DMPE achieved Chamfer Distance 5.79 from four projections with known correspondences; see Tab. 6. These results should not be interpreted as a direct benchmark comparison, but rather as evidence that reliable correspondence extraction remains a central challenge for integrating 3DMPE into an end-to-end image-based reconstruction pipeline.

Table 6: ShapeNet chair reconstruction using COLMAP and 3DMPE.

Pipeline	Input	# Perspectives	Reconstruction	EMD	CD
COLMAP		250		19.7	23.1
3DMPE		4		5.09	5.79

4.5 Implementation Details

We implemented 3DMPE in Python. Our implementation relies on the `pyoint` package for ICP alignment and on the `scikit-learn` manifold module for baseline methods. Numerical computations were performed using `NumPy`, `SciPy`, and `pandas`. We used `trimesh` for reading and sampling both the ShapeNet and Pix3D datasets, and TensorFlow for the alignment algorithm.

We conducted approximately 11,000 experiments across different parameter settings. The source code is available at <https://github.com/rahatzamancse/3DMPE>.

5 Conclusions, Limitations, and Future Work

We presented 3DMPE, a training-free method for reconstructing a 3D point cloud from two or more partially observed 2D projections with cross-view point correspondences. We considered fixed-projection and variable-projection settings, in which the projection maps are known or jointly estimated, respectively. Experiments on ShapeNet and Pix3D evaluated reconstruction quality under varying initialization schemes, numbers of views, levels of point visibility, and noise in distances and correspondences.

A primary limitation of 3DMPE is its assumption that cross-view point correspondences are available. Thus, 3DMPE is not an end-to-end image-to-3D reconstruction method; rather, it addresses the geometric reconstruction stage after correspondence estimation. In preliminary experiments using correspondences obtained from a COLMAP-based pipeline [36], unreliable feature matches produced inputs that were insufficient for accurate reconstruction. Although our controlled experiments demonstrate robustness to local correspondence perturbations, integrating 3DMPE with robust feature matching, tracking, and camera-estimation methods remains an important direction for future work. At the same time, 3DMPE provides a flexible reconstruction module that does not require category-specific training data.

References

1. Altingövde, O., Mishchuk, A., Ganeeva, G., Oveisi, E., Hebert, C., Fua, P.: 3d reconstruction of curvilinear structures with stereo matching deep convolutional neural networks. *Ultramicroscopy* **234**, 113460 (2022)

2. Berger, M., Tagliasacchi, A., Seversky, L.M., Alliez, P., Guennebaud, G., Levine, J.A., Sharf, A., Silva, C.T.: A survey of surface reconstruction from point clouds. *Comput. Graph. Forum* **36**(1), 301–329 (2017)
3. Bianco, S., Ciocca, G., Marelli, D.: Evaluating the performance of structure from motion pipelines. *J. Imaging* **4**(8), 98 (2018)
4. Chang, A.X., Funkhouser, T.A., Guibas, L.J., Hanrahan, P., Huang, Q., Li, Z., Savarese, S., Savva, M., Song, S., Su, H., Xiao, J., Yi, L., Yu, F.: Shapenet: An information-rich 3d model repository. *CoRR* **abs/1512.03012** (2015)
5. Cheng, W.C.: Neural-network-based photometric stereo for 3d surface reconstruction. In: *The 2006 IEEE International Joint Conference on Neural Network Proceedings*. pp. 404–410 (2006). <https://doi.org/10.1109/IJCNN.2006.246710>
6. Choy, C.B., Xu, D., Gwak, J., Chen, K., Savarese, S.: 3d-r2n2: A unified approach for single and multi-view 3d object reconstruction. In: *Computer Vision - ECCV 2016 - 14th European Conference, Amsterdam, The Netherlands, October 11-14, 2016, Proceedings, Part VIII. Lecture Notes in Computer Science*, vol. 9912, pp. 628–644. Springer (2016)
7. Community, B.O.: Blender - a 3D modelling and rendering package. Blender Foundation, Stichting Blender Foundation, Amsterdam (2018), <http://www.blender.org>
8. Deul, C., Burger, M., Hildenbrand, D., Koch, A.: Raytracing point clouds using geometric algebra. In: *submitted to the proceedings of the GraVisMa workshop, Plzen. Citeseer* (2010)
9. Fan, H., Su, H., Guibas, L.J.: A point set generation network for 3d object reconstruction from a single image. In: *2017 IEEE Conference on Computer Vision and Pattern Recognition, CVPR 2017, Honolulu, HI, USA, July 21-26, 2017*. pp. 2463–2471. IEEE Computer Society (2017)
10. Fischler, M.A., Bolles, R.C.: Random sample consensus: A paradigm for model fitting with applications to image analysis and automated cartography. *Commun. ACM* **24**(6), 381395 (jun 1981). <https://doi.org/10.1145/358669.358692>, <https://doi.org/10.1145/358669.358692>
11. Girdhar, R., Fouhey, D.F., Rodriguez, M., Gupta, A.: Learning a predictable and generative vector representation for objects. In: *Computer Vision - ECCV 2016 - 14th European Conference, Amsterdam, The Netherlands, October 11-14, 2016, Proceedings, Part VI. Lecture Notes in Computer Science*, vol. 9910, pp. 484–499. Springer (2016)
12. Hamid, M.S., Manap, N., Hamzah, R.A., Kadmin, A.F.: Stereo matching algorithm based on hybrid convolutional neural network and directional intensity difference. *Artificial intelligence (AI)* **14**, 16 (2021)
13. Häming, K., Peters, G.: The structure-from-motion reconstruction pipeline - a survey with focus on short image sequences. *Kybernetika* **46**(5), 926–937 (2010)
14. Han, X., Laga, H., Bennamoun, M.: Image-based 3d object reconstruction: State-of-the-art and trends in the deep learning era. *IEEE Trans. Pattern Anal. Mach. Intell.* **43**(5), 1578–1604 (2021)
15. Hartley, A., Zisserman, A.: *Multiple view geometry in computer vision* (2. ed.). Cambridge University Press (2006)
16. Hossain, M.I., Huroyan, V., Kobourov, S.G., Navarrete, R.: Multi-perspective, simultaneous embedding. *IEEE Trans. Vis. Comput. Graph.* **27**(2), 1569–1579 (2021)
17. Insafutdinov, E., Dosovitskiy, A.: Unsupervised learning of shape and pose with differentiable point clouds. In: *Advances in Neural Information Processing Systems*

- 31: Annual Conference on Neural Information Processing Systems 2018, NeurIPS 2018, December 3-8, 2018, Montréal, Canada. pp. 2807–2817 (2018)
18. Kar, A., Häne, C., Malik, J.: Learning a multi-view stereo machine. In: Advances in Neural Information Processing Systems 30: Annual Conference on Neural Information Processing Systems 2017, December 4-9, 2017, Long Beach, CA, USA. pp. 365–376 (2017)
 19. Klovov, R., Verbeek, J., Boyer, E.: Probabilistic reconstruction networks for 3d shape inference from a single image. In: 30th British Machine Vision Conference, BMVC 2019, Cardiff, UK, September 9-12, 2019. p. 165. BMVA Press (2019)
 20. Kulon, D., Wang, H., Güler, R.A., Bronstein, M.M., Zafeiriou, S.: Single image 3d hand reconstruction with mesh convolutions. In: 30th British Machine Vision Conference 2019, BMVC 2019, Cardiff, UK, September 9-12, 2019. p. 45. BMVA Press (2019)
 21. Lei, J., Sridhar, S., Guerrero, P., Sung, M., Mitra, N.J., Guibas, L.J.: Pix2surf: Learning parametric 3d surface models of objects from images. In: Computer Vision - ECCV 2020 - 16th European Conference, Glasgow, UK, August 23-28, 2020, Proceedings, Part XVIII. Lecture Notes in Computer Science, vol. 12363, pp. 121–138. Springer (2020)
 22. Leroy, V., Cabon, Y., Revaud, J.: Grounding image matching in 3d with mast3r. In: Computer Vision - ECCV 2024 - 18th European Conference, Milan, Italy, September 29-October 4, 2024, Proceedings, Part LXXII. Lecture Notes in Computer Science, vol. 15130, pp. 71–91. Springer (2024)
 23. Lin, C., Kong, C., Lucey, S.: Learning efficient point cloud generation for dense 3d object reconstruction. In: Proceedings of the Thirty-Second AAAI Conference on Artificial Intelligence, (AAAI-18), the 30th innovative Applications of Artificial Intelligence (IAAI-18), and the 8th AAAI Symposium on Educational Advances in Artificial Intelligence (EAAI-18), New Orleans, Louisiana, USA, February 2-7, 2018. pp. 7114–7121. AAAI Press (2018)
 24. Lowe, D.G.: Object recognition from local scale-invariant features. In: Proceedings of the International Conference on Computer Vision, Kerkyra, Corfu, Greece, September 20-25, 1999. pp. 1150–1157. IEEE Computer Society (1999)
 25. Malitsky, Y., Mishchenko, K.: Adaptive gradient descent without descent. In: Proceedings of the 37th International Conference on Machine Learning, ICML 2020, 13-18 July 2020, Virtual Event. Proceedings of Machine Learning Research, vol. 119, pp. 6702–6712. PMLR (2020)
 26. Mandikal, P., L., N.K., Agarwal, M., Radhakrishnan, V.B.: 3d-lmnet: Latent embedding matching for accurate and diverse 3d point cloud reconstruction from a single image. In: British Machine Vision Conference 2018, BMVC 2018, Newcastle, UK, September 3-6, 2018. p. 55. BMVA Press (2018)
 27. Mandikal, P., Radhakrishnan, V.B.: Dense 3d point cloud reconstruction using a deep pyramid network. In: IEEE Winter Conference on Applications of Computer Vision, WACV 2019, Waikoloa Village, HI, USA, January 7-11, 2019. pp. 1052–1060. IEEE (2019)
 28. Michalkiewicz, M., Belilovsky, E., Baktashmotlagh, M., Eriksson, A.P.: A simple and scalable shape representation for 3d reconstruction. In: 31st British Machine Vision Conference, BMVC 2020, Virtual Event, UK, September 7-10, 2020. BMVA Press (2020)
 29. Miclea, V.C., Nedeveschi, S.: Real-time semantic segmentation-based stereo reconstruction. *IEEE Transactions on Intelligent Transportation Systems* **21**(4), 1514–1524 (2020). <https://doi.org/10.1109/TITS.2019.2913883>

30. Neubert, J., Hammond, T., Guse, N., Do, Y., Hu, Y., Ferrier, N.: Automatic training of a neural net for active stereo 3d reconstruction. In: Proceedings 2001 ICRA. IEEE International Conference on Robotics and Automation (Cat. No.01CH37164) (2001)
31. Özyesil, O., Voroninski, V., Basri, R., Singer, A.: A survey of structure from motion. *Acta Numer.* **26**, 305–364 (2017)
32. Robbins, H., Monro, S.: A Stochastic Approximation Method. *The Annals of Mathematical Statistics* **22**(3), 400 – 407 (1951)
33. Rocco, I., Arandjelovic, R., Sivic, J.: Convolutional neural network architecture for geometric matching. In: Proceedings of the IEEE Conference on Computer Vision and Pattern Recognition (CVPR) (July 2017)
34. Rubner, Y., Tomasi, C., Guibas, L.J.: The earth mover’s distance as a metric for image retrieval. *Int. J. Comput. Vis.* **40**(2), 99–121 (2000)
35. Schoenberger, J.L.: 4 datasets in colmap documentation (2023), <https://colmap.github.io/datasets.html>
36. Schönberger, J.L., Frahm, J.: Structure-from-motion revisited. In: CVPR. pp. 4104–4113 (2016)
37. Seki, A., Pollefeys, M.: Sgm-nets: Semi-global matching with neural networks. In: Proceedings of the IEEE Conference on Computer Vision and Pattern Recognition (CVPR) (July 2017)
38. Shepard, R.N.: The analysis of proximities: multidimensional scaling with an unknown distance function. *Psychometrika* **27**(2), 125–140 (1962)
39. Shirley, P.: Realistic ray tracing. A K Peters (2000)
40. Shrestha, R., Hu, S., Gou, M., Liu, Z., Tan, P.: A real world dataset for multi-view 3d reconstruction. In: Avidan, S., Brostow, G.J., Cissé, M., Farinella, G.M., Hassner, T. (eds.) *Computer Vision - ECCV 2022 - 17th European Conference, Tel Aviv, Israel, October 23-27, 2022, Proceedings, Part VIII. Lecture Notes in Computer Science*, vol. 13668, pp. 56–73. Springer (2022)
41. Sridhar, S., Rempe, D., Valentin, J., Bouaziz, S., Guibas, L.J.: Multiview aggregation for learning category-specific shape reconstruction. In: *Advances in Neural Information Processing Systems 32*, Vancouver, BC, Canada. pp. 2348–2359 (2019)
42. Stewart, G.W.: On the early history of the singular value decomposition. *SIAM Rev.* **35**(4), 551–566 (1993)
43. Sun, X., Wu, J., Zhang, X., Zhang, Z., Zhang, C., Xue, T., Tenenbaum, J.B., Freeman, W.T.: Pix3d: Dataset and methods for single-image 3d shape modeling. In: *2018 IEEE Conference on Computer Vision and Pattern Recognition, CVPR 2018, Salt Lake City, UT, USA, June 18-22, 2018*. pp. 2974–2983. Computer Vision Foundation / IEEE Computer Society (2018)
44. Tatarchenko, M., Dosovitskiy, A., Brox, T.: Octree generating networks: Efficient convolutional architectures for high-resolution 3d outputs. In: *IEEE International Conference on Computer Vision, ICCV 2017, Venice, Italy, October 22-29, 2017*. pp. 2107–2115. IEEE Computer Society (2017)
45. Tulsiani, S., Zhou, T., Efros, A.A., Malik, J.: Multi-view supervision for single-view reconstruction via differentiable ray consistency. In: *2017 IEEE Conference on Computer Vision and Pattern Recognition, CVPR 2017, Honolulu, HI, USA, July 21-26, 2017*. pp. 209–217. IEEE Computer Society (2017)
46. Wang, J., Chen, M., Karaev, N., Vedaldi, A., Rupprecht, C., Novotný, D.: VGGT: visual geometry grounded transformer. In: *IEEE/CVF Conference on Computer Vision and Pattern Recognition, CVPR 2025, Nashville, TN, USA, June 11-15, 2025*. pp. 5294–5306. Computer Vision Foundation / IEEE (2025)

47. Wang, S., Leroy, V., Cabon, Y., Chidlovskii, B., Revaud, J.: Dust3r: Geometric 3d vision made easy. In: IEEE/CVF Conference on Computer Vision and Pattern Recognition, CVPR 2024, Seattle, WA, USA, June 16-22, 2024. pp. 20697–20709. IEEE (2024)
48. Weisstein, E.W.: Triangle point picking. <https://mathworld.wolfram.com/> (1999)
49. Wu, J., Zhang, C., Xue, T., Freeman, B., Tenenbaum, J.: Learning a probabilistic latent space of object shapes via 3d generative-adversarial modeling. In: Advances in Neural Information Processing Systems 29: Annual Conference on Neural Information Processing Systems, Barcelona, Spain. pp. 82–90 (2016)
50. Wu, Z., Song, S., Khosla, A., Yu, F., Zhang, L., Tang, X., Xiao, J.: 3d shapenets: A deep representation for volumetric shapes. In: IEEE Conference on Computer Vision and Pattern Recognition, CVPR 2015, Boston, MA, USA, June 7-12, 2015. pp. 1912–1920. IEEE Computer Society (2015)
51. Yao, Y., Rosasco, L., Caponnetto, A.: On early stopping in gradient descent learning. *Constructive Approximation* **26**(2), 289–315 (2007)
52. Yu, Z., Yang, L., Chen, S., Yao, A.: Local and global point cloud reconstruction for 3d hand pose estimation. In: 32nd British Machine Vision Conference 2021, BMVC 2021, Online, November 22-25, 2021. p. 388. BMVA Press (2021)
53. Zbontar, J., LeCun, Y.: Stereo matching by training a convolutional neural network to compare image patches. *CoRR* **abs/1510.05970** (2015)
54. Zhang, J., Yao, Y., Deng, B.: Fast and robust iterative closest point. *IEEE Trans. Pattern Anal. Mach. Intell.* **44**(7), 3450–3466 (2022)
55. Zheng, J.X., Pawar, S., Goodman, D.F.M.: Graph drawing by stochastic gradient descent. *IEEE Trans. Vis. Comput. Graph.* **25**(9), 2738–2748 (2019)
56. Zhu, H., Jiao, L., Ma, W., Liu, F., Zhao, W.: A novel neural network for remote sensing image matching. *IEEE Transactions on Neural Networks and Learning Systems* (2019)
57. Zhu, Z., Iglesias, A., Zhou, L., You, L., Zhang, J.: Pde-based 3d surface reconstruction from multi-view 2d images. *Mathematics* **10**(4), 542 (2022)

Appendix

Alternative Computation of the ROA Metric

In Sec. 3.3, we proposed the CD, EMD, and ROA metrics for evaluation. In addition to the iterative approach for computing ROA, here we discuss how one can compute the ROA using Singular Value Decomposition (SVD). In our experiments, both the iterative approach and SVD approach described below produce similar results, although the SVD approach takes a bit longer to compute. The idea is as follows: We start by mean shifting both point clouds to the origin. That is, compute

$$\mu_X = \frac{1}{N} \sum_{i=1}^N X_i, \quad \mu_{\hat{X}} = \frac{1}{N} \sum_{i=1}^N \hat{X}_i \quad (13)$$

and subtract them from the corresponding point clouds. We further compute the following matrix:

$$H = (X - \mu_X)(\hat{X} - \mu_{\hat{X}})^T.$$

We continue by computing the Singular Value Decomposition (SVD) [42] of H ,

$$[U, S, V] = SVD(H) \quad (14)$$

We proceed by computing the rotation matrix $R \in \mathbb{R}_{3 \times 3}$

$$R = VU^T \quad (15)$$

and the translation matrix

$$t = \mu_{\hat{X}} - R \times \mu_X \quad (16)$$

In this process, X and \hat{X} are the two point clouds to be aligned and R and t are the computed rotation and translation matrices for aligning the point clouds. We compute ROA values for several ShapeNet examples, using different numbers of perspectives while changing the number of viewpoints from which each point is visible, for both fixed and variable projections; see Fig. 15. The results are consistent with those based on the CD and EMD (Fig. 7 and Fig. 8) metric – 3D reconstruction is very accurate, as long as most points are visible from 3 or more viewpoints.

We also compute ROA values when varying number of points given as input to the reconstruction; see Fig. 16. Here again the results are consistent with those based on the CD and EMD measures (Fig. 6).

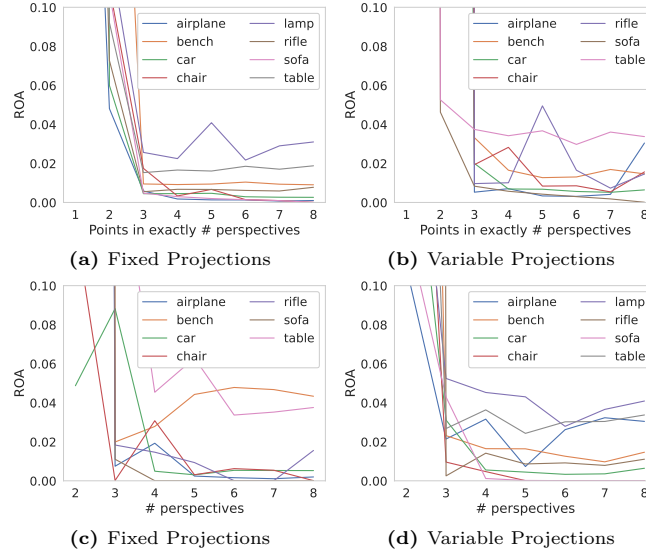


Fig. 15: ROA Metric analysis of 3DMPE on ShapeNet dataset for (a-b) points visible in a number of viewpoints and (c-d) varying number of viewpoints. All experiments are done for 512 points with 8 viewpoints. For (c-d) each point is visible 1 less than the number of viewpoints (except 2 and 3 where all points are visible).

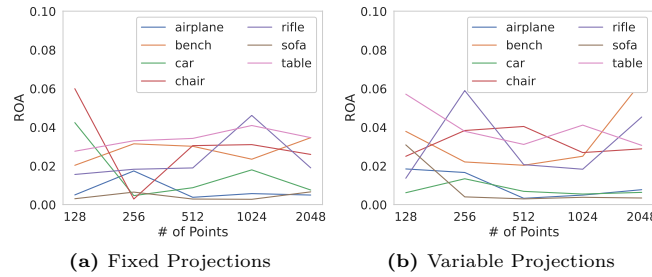


Fig. 16: ROA metrics on a varying number of points on ShapeNet dataset (similar to figure 6a and 6b). Each experiment is done with 4 viewpoints and each point is visible from at least 3 viewpoints.